

Research Article

Group Sparse Basis Pursuit Denoising Reconstruction Algorithm for Polarimetric Through-the-Wall Radar Imaging

Lele Qu , Shimiao An, Tianhong Yang, and Yanpeng Sun

College of Electronic Information Engineering, Shenyang Aerospace University, Shenyang 110136, China

Correspondence should be addressed to Lele Qu; lele83.qu@gmail.com

Received 1 February 2018; Revised 9 May 2018; Accepted 13 June 2018; Published 12 August 2018

Academic Editor: Angelo Liseno

Copyright © 2018 Lele Qu et al. This is an open access article distributed under the Creative Commons Attribution License, which permits unrestricted use, distribution, and reproduction in any medium, provided the original work is properly cited.

Polarimetric through-the-wall radar imaging (TWRI) system has the enhancing performance in the detection, imaging, and classification of concealed targets behind the wall. We propose a group sparse basis pursuit denoising- (BPDN-) based imaging approach for polarimetric TWRI system in this paper. The proposed imaging method combines the spectral projection gradient L1-norm (SPGL1) algorithm with the nonuniform fast Fourier transform (NUFFT) technique to implement the imaging reconstruction of observed scene. The experimental results have demonstrated that compared to the existing compressive sensing- (CS-) based imaging algorithms, the proposed NUFFT-based SPGL1 algorithm can significantly reduce the required computer memory and achieve the improved imaging reconstruction performance with the high computational efficiency.

1. Introduction

Through-the-wall radar imaging (TWRI) based on ultrawideband (UWB) technology has received the substantial attention in recent years. TWRI technology has a large variety of application areas such as urban battle, counterterrorism, and disaster rescue [1]. Benefiting from different responses of a target under diverse polarizations, polarimetric TWRI measurements have shown the improved ability for the detection, localization, and classification of concealed targets behind the wall [2–5].

In order to achieve high-resolution imaging result in the downrange and crossrange, the polarimetric TWRI system is required to utilize the ultrawideband signal and large antenna aperture, which implies the challenge in the acquisition and processing of large amounts of imaging data. Recently, several imaging algorithms based on compressive sensing (CS) technique have been developed for polarimetric TWRI system to reduce the polarimetric measurement data and enhance the imaging quality. In [6], the multitask Bayesian CS (MT-BCS) framework is employed to simultaneously reconstruct the images associated with all polarimetric channels and provide the enhanced image quality compared to the imaging results formed individually for each polarization

channel. A modified clustered MT-BCS algorithm which combines the multipolarization sensing group sparsity and spatially clustered sparsity is proposed in [7] to achieve enhanced imaging capability for extended targets. In [8], a greedy algorithm called look-ahead hybrid matching pursuit (LAHMP) is proposed to provide composite multipolarization imaging result with higher quality. A low-rank and jointly sparse imaging approach [9] is applied to polarimetric TWRI, which achieves the wall clutter mitigation and imaging formation in a unified framework. Although the aforementioned CS-based imaging approaches have been successfully applied to polarimetric TWRI system, these imaging algorithms require that the dictionary matrix should be explicitly constructed before the imaging process and thus are quite computationally intensive with huge memory burden, which severely limits the practical applications of these algorithms to large-scale polarimetric TWRI scenarios.

The contribution of this paper is twofold. First, by exploiting the joint sparsity model, the polarimetric TWRI formation problem is formulated as the group sparse basis pursuit denoising (BPDN) problem, which is solved by the spectral projection gradient L1-norm (SPGL1) algorithm [10, 11]. Second, due to the function handle operation of SPGL1 solver, the type-III nonuniform fast Fourier

transform (NUFFT) technique [12] is exploited to compute the matrix-vector multiplication and avoid the explicit enumeration of dictionary matrix, which can significantly reduce the computer memory requirement and computational complexity in the imaging process. Experimental results have shown that the proposed NUFFT-based SPGL1 imaging algorithm can provide the enhanced imaging performance with the dramatic reduction of required computer memory and computational complexity.

The remainder of this paper is organized as follows. The polarimetric TWRI signal model is outlined in Section 2. The proposed NUFFT-based SPGL1 algorithm to solve group sparse BPDN problem for polarimetric TWRI system is described in Section 3. Section 4 provides experimental results to validate the effectiveness of the proposed imaging method. Section 5 concludes this paper.

2. Signal Model

Consider a two-dimensional (2-D) geometry of the polarimetric TWRI problem, as depicted in Figure 1. The polarimetric TWRI system employs the bistatic measurement configuration, where one antenna transmits and receives the horizontal polarization signal and the other antenna transmits and receives the vertical polarization signal. The two antennas separated by a fixed distance move along the observation line parallel to the x -axis with fixed spatial step. Due to the bistatic measurement configuration, the round-trip propagation path is different for different polarimetric channels at each measurement position. The polarimetric TWRI problem is formulated assuming the stepped-frequency continuous-wave (SFCW) radar operation. The observed scene is partitioned into Q pixels in the crossrange and downrange. Considering a total of M antenna locations and a stepped-frequency signal consisting of N frequencies equispaced over the desired bandwidth, the received signal at the m th ($m = 0, 1, \dots, M - 1$) antenna location and n th ($n = 0, 1, \dots, N - 1$) frequency corresponding to the l th ($l = 1, 2, \dots, L$) polarimetric channel can be expressed as

$$r_{m,l}(n) = \sum_{q=0}^{Q-1} \sigma_l(q) \exp(-j2\pi f_n \tau_{mq,l}), \quad (1)$$

where $\sigma_l(q)$ is the complex reflectivity of the q th pixel corresponding to the l th polarimetric channel, $f_n = f_0 + n\Delta f$ is the n th working frequency, f_0 is the starting frequency, Δf is the uniform frequency step, and $\tau_{mq,l}$ is the round-trip propagation time between the m th antenna location and the q th pixel location $\mathbf{r}_q = (x_q, y_q)$ associated with the l th polarization channel. Given the exact knowledge of the wall permittivity and thickness, $\tau_{mq,l}$ is calculated by the Snell's law [13]. It is also noted that the target reflectivity $\sigma_l(q)$ is assumed to be independent of frequency and aspect angle for each polarization channel.

The discrete version of signal model in (1) can be expressed in matrix-vector form as

$$\mathbf{r}_{m,l} = \mathbf{\Psi}_{m,l} \boldsymbol{\sigma}_l, \quad (2)$$

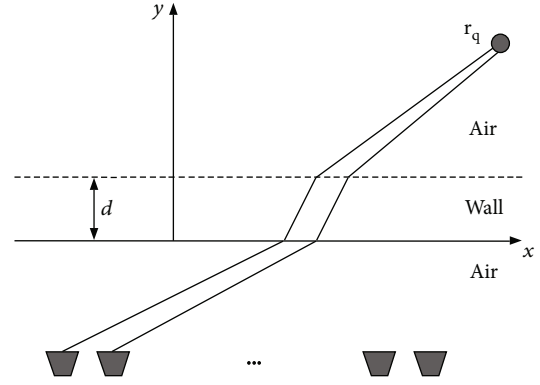


FIGURE 1: 2-D geometry of the polarimetric TWRI problem.

where $\mathbf{r}_{m,l} = [r_{m,l}(0), r_{m,l}(1), \dots, r_{m,l}(N - 1)]^T$ is the measured data vector corresponding to the m th antenna and the l th polarization channel, $\boldsymbol{\sigma}_l = [\sigma_l(0), \sigma_l(1), \dots, \sigma_l(Q - 1)]^T$ is the scene reflectivity vector associated with the l th polarimetric channel, and $\mathbf{\Psi}_{m,l}$ is the $N \times Q$ matrix whose n th row is given by

$$[\mathbf{\Psi}_{m,l}]_n = [e^{-j2\pi f_n \tau_{m0,l}}, \dots, e^{-j2\pi f_n \tau_{mq,l}}, \dots, e^{-j2\pi f_n \tau_{m(Q-1),l}}]. \quad (3)$$

The data model in (2) involves the full set of measurements made at all M antenna locations using N frequencies for each polarization. In TWRI scenarios, the number of point targets is typically much smaller than the number of scene pixels and thus the scene reflectivity vector $\boldsymbol{\sigma}_l$ is a sparse vector. Towards the objective of fast data acquisition, only M_1 ($M_1 < M$) antenna locations and N_1 ($N_1 < N$) frequency bins are randomly selected for each polarization channel. Assume that $m_g \in [0, 1, \dots, M - 1]$ for $g = 0, 1, \dots, M_1 - 1$ and $n_h \in [0, 1, \dots, N - 1]$ for $h = 0, 1, \dots, N_1 - 1$ are the indexes of the selected antenna locations and frequency bins, respectively. At the m_g th antenna location for the l th polarization, consider an undersampled measurement vector $\mathbf{y}_{m_g,l}$, which is a vector of length N_1 composed of elements selected from $\mathbf{r}_{m_g,l}$ as follows:

$$\mathbf{y}_{m_g,l} = \mathbf{\Phi}_{m_g,l} \mathbf{r}_{m_g,l} = \mathbf{\Phi}_{m_g,l} \mathbf{\Psi}_{m_g,l} \boldsymbol{\sigma}_l = \mathbf{A}_{m_g,l} \boldsymbol{\sigma}_l, \quad (4)$$

where $\mathbf{\Phi}_{m_g,l}$ is the $N_1 \times N$ matrix obtained by randomly choosing N_1 rows from the $N \times N$ identity matrix, $\mathbf{A}_{m_g,l} = \mathbf{\Phi}_{m_g,l} \mathbf{\Psi}_{m_g,l}$ is the $N_1 \times Q$ dictionary matrix, and its (h, q) th element is given by

$$[\mathbf{A}_{m_g,l}]_{h,q} = \exp(-j2\pi f_{m_g,l}(n_h) \tau_{m_g,q,l}), \quad (5)$$

where $f_{m_g,l}(n_h) = f_0 + n_h \Delta f$ is the n_h th frequency corresponding to the m_g th antenna location and the l th polarization channel and $\tau_{m_g,q,l}$ is the two-way traveling time between the m_g th antenna and the q th pixel associated with

the l th polarization channel. It is noted that $f_{m_g,l}(n_h)$ is uniformly spaced at each of available antenna locations.

Considering that there are total M_1 available antenna locations for each polarization, we can obtain the linear system of equation as

$$\mathbf{y}_l = \mathbf{A}_l \boldsymbol{\sigma}_l + \mathbf{n}_l, \quad (6)$$

where $\mathbf{y}_l = [\mathbf{y}_{m_0,l}^T, \mathbf{y}_{m_1,l}^T, \dots, \mathbf{y}_{m_{(M_1-1)},l}^T]^T$ and $\mathbf{A}_l = [\mathbf{A}_{m_0,l}^T, \mathbf{A}_{m_1,l}^T, \dots, \mathbf{A}_{m_{(M_1-1)},l}^T]^T$. Without loss of generality, the noise vector \mathbf{n}_l is added in (6) to account for the measurement noise.

3. Proposed Imaging Algorithm

In this section, we propose the group sparse BPDN-based imaging approach for polarimetric TWRI system by combining the SPGL1 algorithm and NUFFT technique to reduce the computer memory requirement and improve the computational efficiency and the imaging performance.

3.1. SPGL1 Group Sparse BPDN Imaging Reconstruction. Commonly, it can be assumed that polarimetric TWRI signals share the same sparsity support over different polarization channels, which means that the position of each point-like target is identical for all polarimetric channels, but its amplitude may be different. As a consequence, all the vectors $\boldsymbol{\sigma}_l$ share the same sparsity pattern for $l = 1, 2, \dots, L$ and the measurement data obtained by different polarization channels can be processed by the multiple measurement vectors (MMV) model. Hence, the sparse solution of $\boldsymbol{\sigma}_l$ can be obtained by solving the group sparse BPDN problem.

$$\begin{aligned} \min \quad & \|\mathbf{X}\|_{1,2} \\ \text{s.t.} \quad & \|\mathbf{A}(\mathbf{X}) - \mathbf{Y}\|_F \leq \eta, \end{aligned} \quad (7)$$

where $\mathbf{X} = [\boldsymbol{\sigma}_1, \boldsymbol{\sigma}_2, \dots, \boldsymbol{\sigma}_L]$, $\mathbf{Y} = [\mathbf{y}_1, \mathbf{y}_2, \dots, \mathbf{y}_L]$, $\mathbf{A}(\mathbf{X}) = [\mathbf{A}_1 \boldsymbol{\sigma}_1, \mathbf{A}_2 \boldsymbol{\sigma}_2, \dots, \mathbf{A}_L \boldsymbol{\sigma}_L]$, $\|\cdot\|_F$ is the Frobenius norm, η is the recovery error tolerance and can be determined by the cross-validation strategy [14], and the mixed (1, 2)-norm $\|\mathbf{X}\|_{1,2}$ is a sum of l_2 -norms of rows of \mathbf{X} , where a row of \mathbf{X} denotes the target reflectivity at a given pixel across different polarimetric channels. Once the solution of \mathbf{X} is obtained, the vectors $\boldsymbol{\sigma}_l$ from different polarimetric channels are combined to form the final composite vector using the additive fusion technique.

$$\boldsymbol{\sigma}_{\text{final}} = \sum_{l=1}^L \frac{|\boldsymbol{\sigma}_l|}{L}. \quad (8)$$

It is noted that the computation burden of (7) is highly dependent on the size of discretized pixels and the number of undersampled measurements. Thus, the polarimetric TWRI reconstruction problem is typically very difficult because of the huge size of dictionary matrix and high computational burden imposed by the polarimetric image formation algorithm. To solve this problem, the proposed imaging

algorithm adopts SPGL1 algorithm to solve the group sparse BPDN problem of (7). The foremost reason for choosing SPGL1 solver is that it can find the solution of group sparse BPDN problem by using functional inputs for dictionary matrix instead of the explicit enumeration of dictionary matrix. The function representation of dictionary matrix can dramatically reduce constraints in creating, storing, and applying the dictionary matrix. In addition, the SPGL1 solver is robust to the model error and noise and has relatively fast computation time.

The basic idea of SPGL1 solver is to reformulate the group sparse BPDN problem of (7) as MMV Lasso (LS_τ) problem

$$\begin{aligned} \min \quad & \|\mathbf{A}(\mathbf{X}) - \mathbf{Y}\|_F \\ \text{s.t.} \quad & \|\mathbf{X}\|_{1,2} \leq \tau. \end{aligned} \quad (9)$$

The MMV LS_τ problem can be solved using the spectral gradient method [10]. In practice, τ is usually not available. For solving this problem, the Pareto curve for the MMV model is defined as

$$\phi(\tau) = \|\mathbf{A}(\mathbf{X}_\tau) - \mathbf{Y}\|_F, \quad (10)$$

where \mathbf{X}_τ is the optimal solution to the MMV LS_τ problem of (9). According to [11], $\phi(\tau)$ is continuously differentiable and $\phi'(\tau_i)$ is expressed as

$$\phi'(\tau_i) = -\frac{\|\mathbf{A}^H[\mathbf{A}(\mathbf{X}_{\tau_i}) - \mathbf{Y}]\|_{\infty,2}}{\|\mathbf{A}(\mathbf{X}_{\tau_i}) - \mathbf{Y}\|_F}, \quad (11)$$

where $\|\cdot\|_{\infty,2}$ is the dual norm of $\|\cdot\|_{1,2}$ and $\mathbf{A}^H(\mathbf{Y}) = [\mathbf{A}_1^H \mathbf{y}_1, \mathbf{A}_2^H \mathbf{y}_2, \dots, \mathbf{A}_L^H \mathbf{y}_L]$. Then, the root of the nonlinear equation $\phi(\tau) = \eta$ can be obtained by Newton iterations.

$$\tau_{i+1} = \tau_i + \frac{\eta - \phi(\tau_i)}{\phi'(\tau_i)}, \quad (12)$$

where τ_0 is usually set as $\tau_0 = 0$, yielding $\phi(0) = \|\mathbf{Y}\|_F$ and $\phi'(0) = -\|\mathbf{A}^H(\mathbf{Y})\|_{\infty,2}/\|\mathbf{Y}\|_F$. It has been proved that with the MMV LS_τ problem being well solved at each iteration, $\phi(\tau)$ can approach η at high speed. We refer the readers to [11, 15] for the detailed description of the operation of SPGL1 solver.

3.2. Implementation of Operators Using NUFFT. In order to use the function handle of SPGL1, the operator formalism is indispensable. The matrix-vector multiplication should be replaced with the specifically designed function to perform the equivalent of the forward operator g_A and adjoint operator g_A^H . Fortunately, the forward operator g_A and adjoint operator g_A^H can be, respectively, implemented using the computationally efficient type-III NUFFT technique [16–18].

The type-III NUFFT algorithm is used to calculate the transformation of nonuniform space data into nonuniform space data. The one-dimensional type-III nonuniform discrete Fourier transform (NUDFT) is defined for Fourier

```

Input:  $\mathbf{A} = [\mathbf{A}_1, \mathbf{A}_2, \dots, \mathbf{A}_L]$ ,  $\mathbf{X} = [\sigma_1, \sigma_2, \dots, \sigma_L]$ 
Output:  $\mathbf{Y} = [Y_1, Y_2, \dots, Y_L]$ 
for  $l = 1 : L$ , do
  for  $g = 0 : M_1 - 1$ , do
    Use the type-III NUFFT technique to calculate (16) and obtain the vector
     $\mathbf{y}_{m_g,l} = [y_{m_g,l}(0), y_{m_g,l}(1), \dots, y_{m_g,l}(N_1 - 1)]^T$ 
  end for
  Reshape  $\mathbf{y}_{m_g,l}$  into the vector  $\mathbf{y}_l = [y_{m_0,l}^T, y_{m_1,l}^T, \dots, y_{m_{(M_1-1)},l}^T]^T$ 
end for
  Put  $\mathbf{y}_l$  into the matrix  $\mathbf{Y}$ 

```

ALGORITHM 1: Forward function algorithm $\mathbf{Y} = g_A(\mathbf{A}, \mathbf{X})$.

coefficients $f_r \in \mathbb{C}$, $r = 0, \dots, R-1$ at arbitrary frequencies $\nu_r \in [-(1/2), 1/2)$ by

$$z_p = \sum_{r=0}^{R-1} f_r e^{-j2\pi F \nu_r a_p} \quad p = 0, \dots, P-1, \quad (13)$$

where $z_p \in \mathbb{C}$ are the samples in the time domain at arbitrary nodes $a_p \in [-(1/2), 1/2)$ and $F \in \mathbb{N}$ is called the nonharmonic bandwidth.

Then the matrix-vector multiplication of $\mathbf{A}_{m_g,l} \sigma_l$ can be written as

$$y_{m_g,l}(h) = \sum_{q=0}^{Q-1} \sigma_l(q) \exp\left(-j2\pi f_{m_g,l}(n_h) \tau_{m_g,q,l}\right). \quad (14)$$

Similarly, the matrix-vector multiplication of $\mathbf{A}_{m_g,l}^H \mathbf{y}_{m_g,l}$ can be expressed as

$$\sigma_{m_g,l}(q) = \sum_{h=0}^{N_1-1} y_{m_g,l}(n_h) \exp\left(j2\pi f_{m_g,l}(n_h) \tau_{m_g,q,l}\right). \quad (15)$$

Equations (14) and (15) can be, respectively, further modified as follows:

$$y_{m_g,l}(h) = \sum_{q=0}^{Q-1} \sigma_l(q) \exp\left(-j2\pi F \hat{f}_{m_g,l}(n_h) \hat{\tau}_{m_g,q,l}\right), \quad (16)$$

$$\sigma_{m_g,l}(q) = \sum_{h=0}^{N_1-1} y_{m_g,l}(n_h) \exp\left(j2\pi F \hat{f}_{m_g,l}(n_h) \hat{\tau}_{m_g,q,l}\right), \quad (17)$$

where $\hat{f}_{m_g,l}(n_h) = c_1 f_{m_g,l}(n_h) \in [-(1/2), 1/2)$ and $\hat{\tau}_{m_g,q,l}(n_h) = c_2 \tau_{m_g,q,l}(n_h) \in [-(1/2), 1/2)$ are scaled versions of the respective variable without a hat. The nonharmonic bandwidth F and scaling constants $c_1, c_2 \in \mathbb{R}$ satisfy the following condition:

$$c_1 c_2 F = 1 \quad F \in \mathbb{N}, \quad (18)$$

where the smallest possible F should be chosen to minimize the computational cost.

It is observed that (16) and (17) both have the similar expression as the definition of (13). Thus, (16) and (17)

can be regarded as the type-III NUDFT and then the forward and adjoint operators can be efficiently calculated by the type-III NUFFT technique. We use the NFFT library [16] to implement the computation of (16) and (17). The detailed procedures on how to perform the forward operator g_A and adjoint operator g_A^H are listed in Algorithms 1 and 2, respectively.

3.3. Computational Complexity and Memory Requirement.

Since there are a total of M_1 available antenna locations for each polarimetric channel, the forward and adjoint operators both involve M_1 evaluations of type-III NUFFT for each polarimetric channel. Thus, the proposed imaging algorithm requires only $O(LM_1(F \log F + |\log \varepsilon|(Q + N_1)))$ floating point operations, where ε is the desired computational accuracy of type-III NUFFT. The traditional CS-based imaging algorithms require the computer memory of $O(LM_1N_1Q)$ to explicitly construct the dictionary matrix. Due to the sophisticated function handle operation, only the randomly selected frequencies and two-way traveling time of each pixel corresponding to M_1 antenna locations and L polarimetric channel should be calculated offline and stored in the memory for the proposed imaging algorithm. Hence, it significantly reduces the required computer memory to $O(LM_1(N_1 + Q))$.

4. Experimental Results

The proposed-based imaging algorithm is evaluated on the experimental TWRI data collected in the Radar Imaging Lab of the Center for Advanced Communications at Villanova University. In the experiment, two horn antennas, one oriented for horizontal polarization and the other oriented for vertical polarization, are used to measure the full polarimetric TWRI signals. The measurement data collected at three polarimetric channels, S11 (HH), S22 (VV), and S12 (HV), are used to evaluate the proposed imaging algorithm. For each polarimetric channel, a 69-element linear array of length 1.5 m is synthesized with an interelement spacing of 0.022 m and a stepped-frequency signal of 1 GHz bandwidth centered at 2.5 GHz with a frequency step size of 5 MHz used to image the scene. The wall is built from a wooden frame, which is fasten with 0.019 m plywood on one side and 0.016 m gypsum wallboard on the other side. The

```

Input:  $\mathbf{A} = [\mathbf{A}_1, \mathbf{A}_2, \dots, \mathbf{A}_L]$ ,  $\mathbf{Y} = [y_1, y_2, \dots, y_L]$ 
Output:  $\mathbf{X} = [\mathbf{A}_1^H y_1, \mathbf{A}_2^H y_2, \dots, \mathbf{A}_L^H y_L]$ 
for  $l = 1 : L$ , do
  for  $g = 0 : M_1 - 1$ , do
    Use the type-III NUFFT technique to calculate (17) and obtain the vector
     $\sigma_{m_g,l} = [\sigma_{m_g,l}(0), \sigma_{m_g,l}(1), \dots, \sigma_{m_g,l}(Q-1)]^T$ 
  end for
  Compute  $\mathbf{A}_l^H y_l = \sum_{g=0}^{M_1-1} \sigma_{m_g,l}$ 
end for
Put  $\mathbf{A}_l^H y_l$  into the matrix  $\mathbf{X}$ 

```

ALGORITHM 2: Adjoint function algorithm $\mathbf{X} = g_A^H(\mathbf{A}, \mathbf{Y})$.

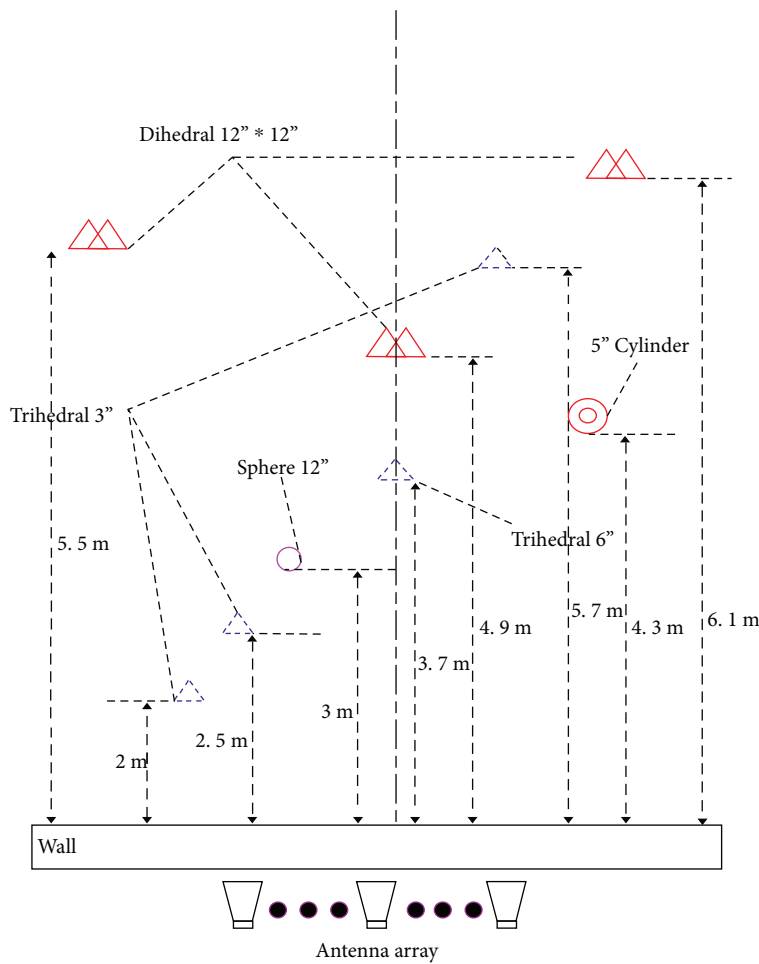


FIGURE 2: True positions of nine targets in the observed scene.

heterogeneous wall has a thickness of 0.127 m and is placed at a standoff distance of 0.0127 m from the front face of the antennas. More detailed information about the experimental setup is provided in [19]. The raw data are preprocessed by the background subtraction procedure to remove the strong antenna coupling and wall reflection signal. The observed scene contains nine targets: a sphere, three dihedrals, four trihedrals, and a cylinder. Figure 2 shows the true positions of nine targets in the observed scene.

The imaged scene extends from 1 m and 6.95 m in the downrange and -2 m and 1.95 m in the crossrange. The pixel size is set to $0.05 \text{ m} \times 0.05 \text{ m}$, which gives the image of size 120×80 pixels. Here, only 100 randomly selected frequency points and 30 randomly selected antenna positions for each polarization channel are employed for imaging reconstruction.

We compare the imaging results of the proposed SPGL1 group sparse BPDN reconstruction algorithm with that of

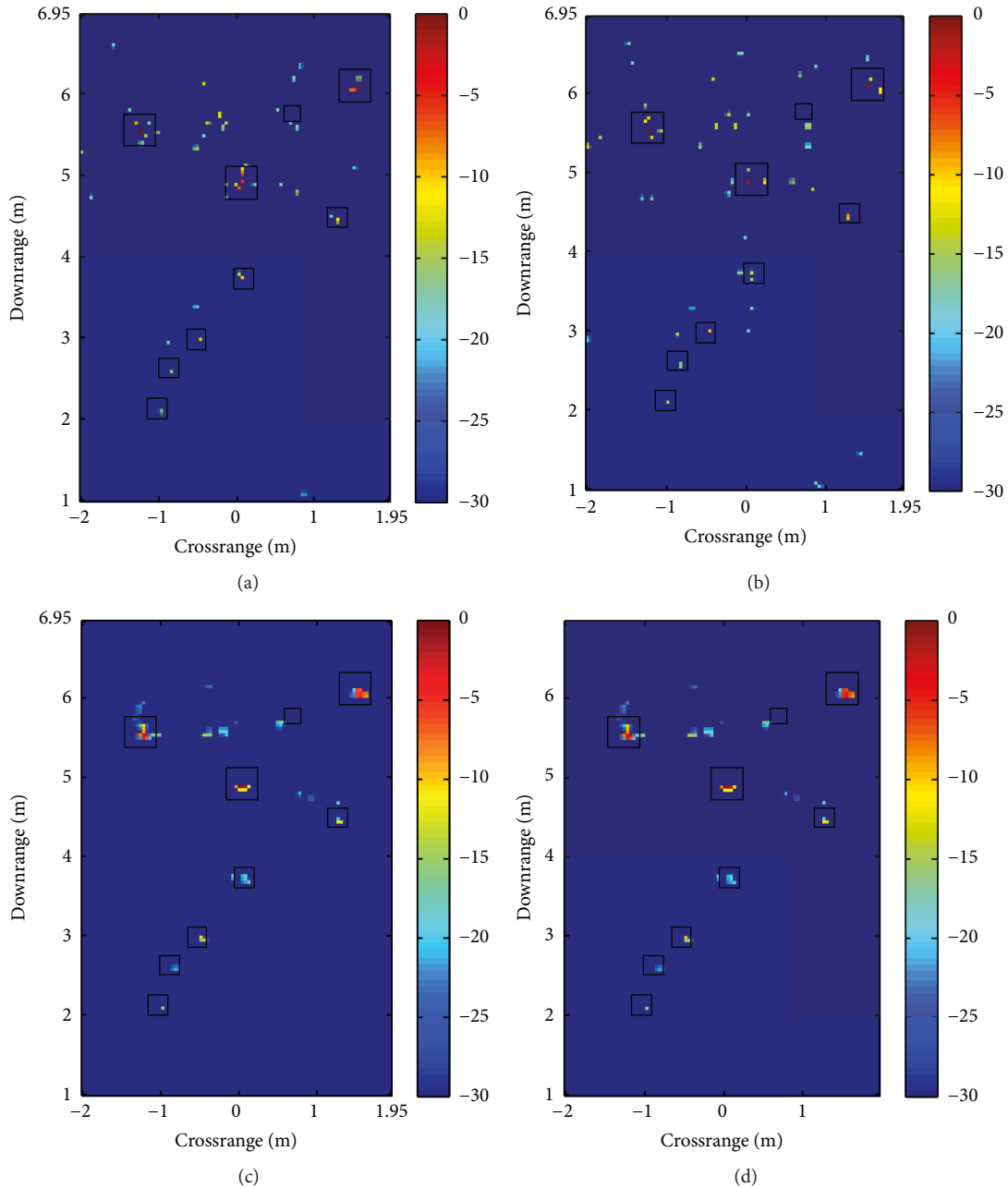


FIGURE 3: The imaging results of four different algorithms. (a) MT-BCS. (b) LAHMP. (c) The traditional SPGL1. (d) The proposed NUFFT-based SPGL1.

the existing MT-BCS and LAHMP algorithms, which use the same inherent spatial sparsity property as the proposed algorithm. The 2-D imaging results of four different algorithms are provided in Figure 3. The images are all normalized to their own maxima and shown on the same 30 dB scale. The true target positions are indicated with black rectangles. Figure 3(a) shows the imaging result obtained by the MT-BCS technique, which requires the prior knowledge about the probability distribution of reflection coefficients of the scene. Figure 3(b) depicts the imaging result based on LAHMP algorithm, which combines the advantage of hybrid matching pursuit with the look-ahead strategy and requires the sparsity level of observed scene in advance. The

sparsity level for LAHMP algorithm is set to 50. The group sparse BPDN-based imaging result obtained by the traditional SPGL1 algorithm with direct matrix-vector multiplication is given in Figure 3(c). The group sparse BPDN-based imaging result using the proposed NUFFT-based SPGL1 algorithm is given in Figure 3(d). In Figures 3(c) and 3(d), the dominant pixels are more concentrated around the target locations and the spurious artifacts outside the target areas are more effectively suppressed. Due to the heterogeneous nature of the wall, the information of wall permittivity and thickness is not exactly known and the distortion of propagation path introduced by the wall is omitted in the imaging process. However, we can still obtain the satisfactory imaging

TABLE 1: Comparison of four algorithms.

Algorithm	TCR (dB)	Running time (sec)	Memory requirement (MB)
MT-BCS	21.05	23.34	2636.8
LAHMP	19.08	180.35	1318.4
The traditional SPGL1 algorithm	25.62	279.68	6.661
The proposed NUFFT-based SPGL1 algorithm	25.62	39.78	6.661

result using the proposed imaging algorithm. So, we can conclude that the proposed imaging approach is robust against the erroneous knowledge of wall parameters to some extent. It is noted that the small dihedral at the downrange of 5.7 m is missed in the reconstructed images of Figure 3, which could be attributed to its weak scattering characteristic. A few clutter which are located outside of target area are caused by the interactions between the wall and targets.

To quantitatively compare the imaging reconstruction performance of these algorithms, the target-to-clutter ratio (TCR) is applied to compare imaging performance. The definition of the TCR is given by

$$\text{TCR} = 10 \lg \left(\frac{1/N_t \sum_{q \in A_t} |I(q)|^2}{1/N_c \sum_{q \in A_c} |I(q)|^2} \right), \quad (19)$$

where $|I(q)|$ is the magnitude of the q th complex-valued pixel of the reconstructed image, A_t is the target area, A_c is the clutter area, and N_t and N_c are the number of pixels in the target and clutter areas, respectively. The target and clutter areas are selected according to the ground-truth locations of the targets [5]. A large value of TCR indicates that the dominant pixels are exactly concentrated at the target areas and the artifacts outside the target areas are effectively suppressed.

We repeat 50 trials on the reduced set of experimental data, where 100 frequency points and 30 antenna locations are randomly selected from each polarimetric channel for each trial. The average TCR, average running time, and computer memory requirement of storage of dictionary matrix of three algorithms are listed in Table 1. All computations are performed by MATLAB 2014 on a laptop with Intel® Core™ I7-4510 U CPU at 2 GHz and 8 GB memory. It can be observed that the group sparse BPDN imaging approach using the SPGL1 algorithm achieves the highest value of TCR, which means that the SPGL1 algorithm has the improved ability of accurate localization of target and effective suppression of spurious artifacts. The SPGL1 algorithm also requires the least computer memory, which dramatically reduces the constraints of memory requirement of creating and applying the dictionary matrix in the imaging formation. In particular, the proposed NUFFT-based SPGL1 algorithm has much less computational time than the traditional SPGL1 algorithm which performs the direct matrix-vector multiplication without the exploitation of the NUFFT technique. This advantage is provided by the computational efficiency of the NUFFT technique in the matrix-vector multiplication.

Table 2 lists the computational complexity of four algorithms. For the MT-BCS algorithm, K is the number of relevant basis functions associated with nonzero weights. For the

TABLE 2: Computational complexity of four algorithms.

Algorithm	Computational complexity
MT-BCS	$O(LK^2Q)$
LAHMP	$O(K^2(K^2 + Q)LM_1N_1)$
The traditional SPGL1 algorithm	$O(LM_1N_1Q)$
The proposed NUFFT-based SPGL1 algorithm	$O(LM_1(F \log F + \log \epsilon (Q + N_1)))$

TABLE 3: TCR of the NUFFT-based SPGL1 algorithm for different percentages of measurements.

Percentage of measurements	TCR (dB)
20%	24.28
30%	25.51
40%	25.96
50%	26.23

LAHMP algorithm, K is the preset sparsity level of the observed scene. From the comparison of the computational complexity, the computational complexity of the proposed NUFFT-based SPGL1 algorithm is significantly reduced compared to the traditional SPGL1 algorithm.

In order to investigate the effect of reducing measurements on the imaging performance of the proposed NUFFT-based SPGL1 algorithm, several reduced datasets accounting for different percentages of the full measurements are generated by randomly selecting measurements at each polarimetric channel. Table 3 presents the TCR values for different reduced datasets, which are averaged by 50 independent trials. It is observed that the TCR slightly increases with the number of measurements used for imaging reconstruction and the proposed algorithm yields good TCR values for all reduced datasets.

5. Conclusion

In this paper, we have proposed a novel NUFFT-based SPGL1 group sparse BPDN reconstruction algorithm for polarimetric TWRI system. The experimental results have demonstrated that compared to the existing CS-based imaging algorithms, the proposed imaging algorithm can significantly reduce the required computer memory and provide the improved imaging quality with the relatively high computational efficiency. Hence, the proposed imaging algorithm is more practical for polarimetric TWRI system.

Data Availability

The data used to support the findings of this study are available from the corresponding author upon request.

Conflicts of Interest

The authors declare that they have no conflicts of interest.

Acknowledgments

The authors would like to thank the Center for Advanced Communications at Villanova University for providing the polarimetric TWRI experimental data. This work was supported in part by the National Natural Science Foundation of China under Grants 61671310 and 61302172, in part by the Aeronautical Science Foundation of China under Grant 2016ZC54013, in part by the Innovative Talents Program of Universities of Liaoning Province under Grant LR2016062, and in part by the Scientific Research Project of the Department of Education of Liaoning Province under Grant L201752.

References

- [1] M. G. Amin, *Through-The-Wall Radar Imaging*, CRC Press, Boca Raton, FL, USA, 2010.
- [2] M. Thiel and K. Sarabandi, "Ultra-wideband multi-static scattering analysis of human movement within buildings for the purpose of stand-off detection and localization," *IEEE Transactions on Antennas and Propagation*, vol. 59, no. 4, pp. 1261–1268, 2011.
- [3] C. Debes, A. M. Zoubir, and M. G. Amin, "Enhanced detection using target polarization signatures in through-the-wall radar imaging," *IEEE Transactions on Geoscience and Remote Sensing*, vol. 50, no. 5, pp. 1968–1979, 2012.
- [4] W. Zhang, A. Hoorfar, C. Thajudeen, and F. Ahmad, "Full polarimetric beam-forming algorithm for through-the-wall radar imaging," *Radio Science*, vol. 46, no. 5, pp. 1–17, 2011.
- [5] C. H. Seng, A. Bouzerdoum, M. G. Amin, and S. L. Phung, "Probabilistic fuzzy image fusion approach for radar through wall sensing," *IEEE Transactions on Image Processing*, vol. 22, no. 12, pp. 4938–4951, 2013.
- [6] A. Bouzerdoum, F. H. C. Tivive, and V. H. Tang, "Multi-polarization through-the-wall radar imaging using joint Bayesian compressed sensing," in *2014 19th International Conference on Digital Signal Processing*, pp. 783–788, Hong Kong, China, August 2014.
- [7] Q. Wu, Y. D. Zhang, F. Ahmad, and M. G. Amin, "Compressive-sensing-based high-resolution polarimetric through-the-wall radar imaging exploiting target characteristics," *IEEE Antennas and Wireless Propagation Letters*, vol. 14, pp. 1043–1047, 2015.
- [8] X. Wang, G. Li, Q. Wan, and R. J. Burkholder, "Look-ahead hybrid matching pursuit for multipolarization through-wall radar imaging," *IEEE Transactions on Geoscience and Remote Sensing*, vol. 55, no. 7, pp. 4072–4081, 2017.
- [9] A. Bouzerdoum, V. H. Tang, and S. L. Phung, "A low-rank and jointly-sparse approach for multipolarization through-wall radar imaging," in *2017 IEEE Radar Conference (RadarConf)*, pp. 263–268, Seattle, WA, USA, May 2017.
- [10] E. van den Berg and M. P. Friedlander, "Probing the Pareto frontier for basis pursuit solutions," *SIAM Journal on Scientific Computing*, vol. 31, no. 2, pp. 890–912, 2009.
- [11] E. van den Berg and M. P. Friedlander, "Sparse optimization with least-squares constraints," *SIAM Journal on Optimization*, vol. 21, no. 4, pp. 1201–1229, 2011.
- [12] J.-Y. Lee and L. Greengard, "The type 3 nonuniform FFT and its applications," *Journal of Computational Physics*, vol. 206, no. 1, pp. 1–5, 2005.
- [13] G. Wang and M. G. Amin, "Imaging through unknown walls using different standoff distances," *IEEE Transactions on Signal Processing*, vol. 54, no. 10, pp. 4015–4025, 2006.
- [14] R. Ward, "Compressed sensing with cross validation," *IEEE Transactions on Information Theory*, vol. 55, no. 12, pp. 5773–5782, 2009.
- [15] E. van den Berg and M. P. Friedlander, "SPGL1: a solver for large-scale sparse reconstruction," 2015, <http://www.cs.ubc.ca/~mpf/spgl1>.
- [16] J. Keiner, S. Kunis, and D. Potts, "Using NFFT3—a software library for various nonequispaced fast Fourier transform," *ACM Transactions on Mathematical Software*, vol. 36, no. 4, pp. 1–30, 2009.
- [17] A. Capozzoli, C. Curcio, A. Liseno, and A. Riccardi, "Parameter selection and accuracy in type-3 non-uniform FFTs based on Gaussian gridding," *Progress In Electromagnetics Research*, vol. 142, pp. 743–770, 2013.
- [18] A. Capozzoli, C. Curcio, A. Liseno, and J. Piccinotti, "Efficient computing of far-field radiation in two dimension," *IEEE Antennas and Wireless Propagation Letters*, vol. 16, pp. 2034–2037, 2017.
- [19] R. Dilsavor, W. Ailes, P. Rush et al., "Experiments on wide-band through-the-wall radar imaging," in *Proceedings Volume 5808, Algorithms for Synthetic Aperture Radar Imagery XII*, pp. 196–209, Orlando, FL, USA, May 2005.



Hindawi

Submit your manuscripts at
www.hindawi.com

